Polymer Journal (2016) 48, 399–406

www.nature.com/pj

ORIGINAL ARTICLE

Orientation and relaxation behaviors of lamellar microdomains of poly(methyl methacrylate)-*b*-poly(*n*-butyl acrylate) thin films as revealed by grazing-incidence small-angle X-ray scattering

Itsuki Saito[1], Daiki Shimada[1], Mayu Aikawa[1], Tsukasa Miyazaki[2], Keisuke Shimokita[2], Hideaki Takagi[3] and Katsuhiro Yamamoto[1]

The orientation behavior and domain spacing relaxation of the phase-separated structure of poly(methyl methacrylate-*b*-*n*-butyl acrylate) (PMMA-P*n*BA) thin films were investigated by grazing-incidence small-angle X-ray scattering (GISAXS). Moreover, low-energy GISAXS (tender X-ray) was performed for the in-depth profiling of the microphase-separated structure. PMMA-P*n*BA forms a lamellar structure. Parallel orientation of the lamellae was induced by thermal annealing. XPS measurements indicated that surface segregation of the P*n*BA component occurred rapidly, within 1 min after annealing at 160 °C. GISAXS measurements revealed that the apparent degree of orientation and the domain spacing $D_{||}$ of the parallel-oriented lamellae increased with annealing time, and the final $D_{||}$ was close to the domain spacing of the bulk material. The domain spacing relaxation took longer than the orientation of the lamellae of the block copolymers. Furthermore, it was found that $D_{||}$ in the vicinity of the surface was greater than inside the film, which indicates that the domain spacing near the surface relaxed faster than inside due to the higher mobility of the polymer chain.
Polymer Journal (2016) **48,** 399–406; doi:10.1038/pj.2016.2; published online 3 February 2016

INTRODUCTION

Block copolymers (BCP) can form diverse structures with a periodicity of several tens of nanometers, both in bulk and in thin films. Recently, BCP thin films have attracted great attention as materials applicable to several fields, for example, nanolithography,[1–3] solar cells,[4–6] size-selective separation[7,8] and adhesive materials.[9,10] In the bulk state, a microphase-separated structure is predicted by the Flory–Huggins interaction parameter, the degree of polymerization and the block volume fraction,[11–13] while in thin film, the film thickness,[14,15] substrate–polymer interaction and polymer–air interaction[16] must also be considered. Although the phase-separation behavior of BCP in thin films is more complicated, controlling the morphology, orientation and size of the structure is necessary for practical use. This need has motivated many studies with respect to orientation control methodologies, such as film thickness,[14,15,17,18] surface free energy,[18–24] surface topology,[19,25–27] external applied fields[28–34] and solvent vapor or thermal annealing.[21,35–42] Because the functionality and physical properties are also strongly related to the structure and the mobility in the vicinity of the interface, a detailed description of the structure is required. Thus, a number of characterization methods, such as atomic force microscopy (AFM), electron microscopy, dynamic secondary ion mass spectrometry (DSIMS), X-ray photoelectron spectroscopy (XPS), grazing-incidence small-angle X-ray or neutron scattering (GISAXS, GISANS) and X-ray or neutron reflectivity (XRR, NR),[17,43–56] have been used to study the structure of BCP thin films.

Gu *et al.*[57] performed an *in situ* GISAXS measurement of a BCP thin film during solvent vapor annealing to reveal the changes in the microphase-separated structure. According to their report, the swelling ratio, that is, the thickness of the swollen film divided by the original thickness, and the solvent removal rate affect not only the domain spacing but also the lateral ordering. Furthermore, the swelling ratio also influences the grain size. Hence, the swelling ratio and solvent removal rate have a key role in structure development during solvent vapor annealing. Albert *et al.*[58] investigated the effects of surface free energy on the wetting behavior of BCP prepared on a Si substrate with a nearly linear gradient of surface free energy. They showed that the wetting behavior of poly(styrene-*b*-methyl methacrylate) on the chemically modified Si substrate strongly depends on the surface free energies. Although many studies related to BCP morphology, orientation, wetting behaviors and so on have been reported, the depth profile of the phase-separation behavior is still unknown. In the

[1]Department of Materials Science and Engineering, Graduate School of Engineering, Nagoya Institute of Technology, Nagoya, Japan; [2]Functional Design Technology Center, Nitto Denko Corporation, Osaka, Japan and [3]Photon Factory, Institute of Materials Structure Science, High Energy Accelerator Research Organization, Ibaraki, Japan
Correspondence: Professor K Yamamoto, Department of Materials Science and Engineering, Graduate School of Engineering, Nagoya Institute of Technology, Gokiso-cho, Showa-ku, Nagoya, Aichi 466-8555, Japan.
E-mail: yamamoto.katsuhiro@nitech.ac.jp
Received 22 October 2015; revised 19 December 2015; accepted 20 December 2015; published online 3 February 2016

phase-separation behavior of BCP thin films, selective segregation at the polymer–substrate and air–polymer interfaces due to the difference of the surface (interfacial) free energy, microdomain orientation and relaxation of domain spacing over different time scales must be taken into account to investigate the structure development. Thus, further precise structural analysis must be conducted. In addition, the higher mobility of polymer chains in the vicinity of the air surface and interactions at the interfaces cause changes to the structure and orientation with increasing depth.[49,59,60] To achieve depth-resolved structure analysis, several approaches have been employed. DSIMS can reveal BCP morphology and polymer chain diffusion with increasing depth.[45,46] Recently, time-of-flight (ToF) SIMS with an ion cluster beam was reported to be a particularly well-suited technique that enables the in-depth profiling of polymers.[61] Müller-Buschbaum and co-workers have developed the GISANS measurement, which possesses depth sensitivity, for BCP thin films.[50,52,62] Moreover, the GISANS measurement provides structure information near not only the air–polymer interface but also the polymer-substrate surface because a neutron beam can propagate into a silicon substrate. SAXS and GISAXS measurements have often been conducted using X-ray energies of 8–13 keV (hard X-ray). However, under this condition, the X-ray penetration depth rapidly reaches micrometer order, which is generally greater than the thickness of the probed films. Near the critical angle of total reflection α_c at the surface, a depth-resolved GISAXS measurement with hard X-rays is impractical. Recently, Okuda *et al.*[63] introduced a depth-sensitive GISAXS technique utilizing soft X-rays with an X-ray energy of 1.77 keV. They investigated the structural relaxation near the surface and the dynamic heterogeneity of polymer chains in thin films with this technique. We have also reported a depth-resolved structure analysis with GISAXS measurement using tender (soft) X-ray.[64] It was revealed that a polystyrene-*b*-poly(2-vinylpyridine) thin film formed a hexagonally close-packed cylinder structure aligned parallel to the surface that deformed along the depth direction in the thin film (thickness 420 nm), while the deformation was relaxed in the vicinity of the surface.

In this report, we use GISAXS measurements to investigate the phase-separation behavior of poly(methyl methacrylate-*b*-*n*-butyl acrylate) (PMMA-P*n*BA) forming a lamellar structure aligned parallel to the substrate after appropriate thermal annealing. Both components of PMMA-P*n*BA possess polarity, and the phase-separated PMMA-P*n*BA is a thermoplastic elastomer. Thus, PMMA-P*n*BA is applicable as a pressure sensitive adhesive (PSA) material. Understanding phase-separation behavior in films (thin films) is essentially important to advance the functionality of PMMA-P*n*BA as a PSA material. Herein, we investigated the structure development through parameters such as the degree of lamellar orientation and the relaxation of the lamellar domain spacing using GISAXS. The time scale of each process was also evaluated. As a result, the time scale of the orientation was found to be shorter than that of the relaxation. Moreover, we also performed GISAXS measurement with tender X-rays for depth-resolved structure analysis. This technique revealed that the domain spacing of the lamellar structure was slightly larger in the vicinity of the air surface and was closer to the value of the bulk state inside the film. This result indicates that the relaxation of the domain spacing is faster near the air surface, arising from the higher mobility of the polymer chains.

MATERIALS AND METHODS

Materials

Methyl methacrylate (MMA), *tert*-butyl acrylate (*t*BA) and *N,N,N′,N″,N″*-pentamethyldiethylenetriamine (PMDETA) were purchased from Sigma-Aldrich Co., Ltd (St Louis, MO, USA), *p*-Toluenesulfonyl chloride (TsCl), CuBr, anisole, 1-butanol, *p*-toluenesulfonic acid monohydrate (PTSA), toluene, *n*-hexane, methanol and tetrahydrofuran (THF) were obtained from Nacalai Tesque (Japan). MMA and *t*BA were purified by distillation over aluminum oxide granules before polymerization, and other reagents were used as received.

Synthesis of PMMA-*b*-P*n*BA

To obtain PMMA-P*n*BA ($M_n = 32\,000$, $M_w/M_n = 1.17$, $f_{PMMA} = 0.44$), poly (methyl methacrylate-*b*-*tert*-butyl acrylate) (PMMA-P*t*BA) was synthesized via atom transfer radical polymerization (ATRP), followed by transesterification. ATRP is known as a powerful tool to synthesize various block copolymers, as comprehensively reviewed elsewhere.[65] Herein, a typical ATRP procedure was used as reported previously.[36,66] MMA, TsCl, CuBr, OMDETA and anisole were added to a round-bottomed flask. The flask was degassed with several freeze–pump–thaw cycles, sealed in vacuum and immersed in an oil bath at 90 °C for 3 h to promote the polymerization reaction. After the reaction time, the flask was exposed to air, and the solution was stirred with active aluminum powder for several hours to remove the catalysts. Subsequently, PMMA macroinitiator was precipitated in a large amount of *n*-hexane, followed by filtration and drying in a vacuum oven. Chain extensions were performed using a similar procedure. PMMA macroinitiator, *t*BA, CuBr, PMDETA and anisole were added to a round-bottom flask. After several freeze–pump–thaw cycles, the flask was sealed and immersed in an oil bath at 100 °C to start polymerization. After 24 h, the PMMA-P*t*BA block copolymer was precipitated in a large volume of a methanol/water (9/1 vol) mixture, followed by drying in a vacuum oven.

Transesterification was conducted to obtain PMMA-P*n*BA. The synthesized PS-P*t*BA, PTSA (0.1 equivalent of *t*BA unit), 1-butanol (10 equivalent of *t*BA unit) and toluene (to fully dissolve the block copolymer) were added to a round-bottom flask. The flask was immersed in an oil bath at 120 °C to promote the transesterification of *t*BA to *n*BA. After 48 h, PMMA-P*n*BA was precipitated in a large amount of methanol, followed by drying in a vacuum oven (the exchange rate was > 99% as revealed by NMR).

To determine the molecular weights and polydispersity indices of the synthesized polymers, size exclusion chromatography (SEC) was performed under the following conditions: in THF (1 ml per min) at 313 K on four polystyrene gel columns (Tosoh TSK, Tokyo, Japan), gel GMH (base size 7 mm) and G400H, G200H and G100H (5 mm), which were connected to a Tosoh CCPE pump (Tosoh) and ERC-7522 RI reactive index detector (ERMA Inc, Tokyo, Japan). The SEC columns were calibrated against standard PMMA (Tosoh) samples.

Proton nuclear magnetic resonance (^{1}H NMR) spectra were recorded with a Bruker 200M NMR instrument with tetramethylsilane (TMS) as the internal standard, using $CDCl_3$ as the solvent at room temperature.

SEC and NMR charts of block copolymer are provided in the Supplementary Figures S1 and S2.

Preparation of thin films

For thin films, 5 wt% polymer solutions were prepared with THF, followed by spin casting on a silicon substrate at 3000 r.p.m. for 30 s. The thin films were dried at room temperature. Subsequently, thermal annealing was performed at 160 °C. The thickness of the thin films was measured to be ~280 ± 30 nm using an Optical Nanogauge C10178-01 optical interferometer (Hamamatsu Photonics, Co., Ltd, Japan).

Grazing-incidence small-angle X-ray scattering

To study the microphase-separated structures in thin films, GISAXS measurements utilizing hard X-ray and tender (soft) X-ray were performed. Hard X-ray GISAXS measurements were conducted at beamlines BL6A and BL10C of the KEK Photon Factory in Tsukuba, Japan, and BL03XU at SPring-8 in Hyogo, Japan,[67,68] with wavelengths of 0.15 (BL6A), 0.1488 (BL10C) and 0.1 nm (BL03XU). At beamlines BL6A and BL10C, PILATUS 1M (Dectris) and PILATUS 2M (Dectris) detectors were used, which were set at positions 2 ~ 3 m from the sample position. In BL03XU, a charge-coupled device with an image intensifier (II-CCD, Hamamatsu Photonics Co., Ltd) was used as the

detector; it was positioned 2 m away from the sample position. Tender X-ray GISAXS measurements were performed at BL15A2 in the KEK Photon Factory. Tender and soft X-ray GISAXS have recently been used as powerful tools for surface-sensitive and depth-resolved structure analysis of thin films.[63,64,69,70] BL15A2 offers X-rays in a wide energy range, from 2.1 to 15 keV (with an energy resolution of 2×10^{-4}). Herein, the X-ray energy was set at 2.40 keV (corresponding to a wavelength of 5.16 Å), and the sample to detector distance was ~830 mm. To record the GISAXS images, PILATUS 2 M, which is designed to operate under vacuum, was used. All detectors were calibrated with lead stearate prepared in-house ($d=5.01$ nm) and chicken tendon collagen ($d=65.3$ nm). The magnitude of the scattering vector is given by $q=4\pi\sin\theta/\lambda$, where λ is the X-ray wavelength and 2θ is the scattering angle. The scattering vector q_z denotes the component perpendicular to the film surface. The q_x and q_y are the scattering vector components in the sample surface, perpendicular to and parallel to the X-ray beam, respectively. For each set $I(y,z)$, the detector pixels are converted into an exit angle α_f perpendicular to the surface and an angle ψ parallel to the surface by simple geometrical considerations, resulting in a set $I(\psi,\alpha_f)$. Using

$$q_x=\left(\frac{2\pi}{\lambda}\right)(\cos\psi\cos\alpha_f-\cos\alpha_i), \tag{1}$$

$$q_y=\left(\frac{2\pi}{\lambda}\right)\sin\psi\sin\alpha_f, \tag{2}$$

and

$$q_z=\left(\frac{2\pi}{\lambda}\right)(\sin\alpha_i+\sin\alpha_f) \tag{3}$$

where α_i is the incident angle that is hereafter defined for convenience as the angle between the incident X-ray and the surface. This data set was further converted into $I(q_y, q_z)$.

We confirmed that both PMMA-P*n*BA thick (1 mm) and thin films (spin cast) formed lamellar morphology with given sufficient annealing temperature and time as indicated in Supplementary Figures S3 (SAXS) and S4 (GISAXS), respectively.

Penetration depth of X-ray. The X-ray penetration depth Λ is defined as the depth at which the X-ray intensity is attenuated by $1/e$. The value of Λ depends on the X-ray energy (in other words, the wavelength λ), the critical angle of total reflection α_c and the angle of incidence α_i. Under this definition, Λ is given by[71]

$$\Lambda=\frac{\lambda}{4\pi}\sqrt{\frac{2}{\sqrt{\left(\alpha_i^2-\alpha_c^2\right)^2+4\beta^2}-\left(\alpha_i^2-\alpha_c^2\right)}}, \tag{4}$$

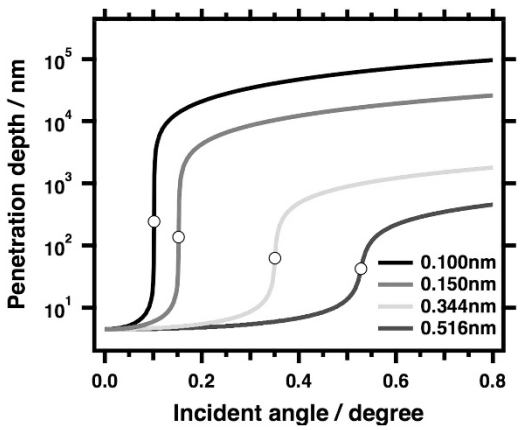

Figure 1 Penetration depth calculated for the present PMMA-P*n*BA film for different X-ray wavelengths (different energies). Symbols indicate the penetration depth at the critical angle of total reflection. A full color version of this figure is available at *Polymer Journal* online.

where β is the imaginary part of the complex refractive index. The critical angle α_i; δ, which specifies the deviation from the real part of the refractive index; and β are given by

$$\alpha_c=\sqrt{2\delta} \tag{5}$$

$$\delta=\left(r_e\lambda^2N_A/2\pi\right)\rho_M\sum_Z w_Z\left(f_{0Z}+f_Z^{'}(E)\right)/\sum_Z w_iA_Z \tag{6}$$

$$\beta=\left(r_e\lambda^2N_A/2\pi\right)\rho_M\sum_Z w_Zf_Z^{''}(E)/\sum_Z w_ZA_Z \tag{7}$$

where r_e is the classical electron radius (2.82×10^{-5} Å), N_A is Avogadro's number, ρ_M is the mass density, w_Z is the fraction of element Z, A_Z is the relative atomic mass, f_{0Z} is the non-resonant term of the atomic scattering factor corresponding to the atomic number, and $f_Z'(E)$ and $f_Z''(E)$are the real and imaginary parts of the anomalous dispersion for the incident X-ray energy E. For example, here we used 4.2503×10^{-5} for δ and 9.4521×10^{-7} for β of P*n*BA at 2.40 keV. Furthermore, using Equation (5), the critical angle of total reflection was calculated to be 0.528°. Figure 1 shows the calculated penetration depth of PMMA-P*n*BA. It is difficult to precisely control the penetration depth Λ at the nanometer scale for a GISAXS experiment conducted using hard X-rays (1.00–1.50 Å) because the value of Λ rises abruptly at α_c. However, it can be seen that as the X-ray energy decreases (wavelength increases), Λ changes more gradually near the critical angle and shows decreased depth values at angles greater than the critical angle. Therefore, better control of Λ is expected for depth-resolved GISAXS measurements using tender X-rays (2.40 keV) because the critical angle and attenuation coefficient values are much larger than those for the hard X-rays.

RESULTS AND DISCUSSION

Orientation and relaxation of lamellar structures

Two-dimensional (2D) GISAXS (hard X-ray) patterns with varying annealing times are summarized in Figure 2. The 2D GISAXS pattern of the as-spun sample (Figure 2a) is shaped like an ellipse, which may arise from poorly ordered or kinetically frozen morphology. Partially intense scattering was observed at q_z values of 0.25–0.28 nm^{-1}, where it was intensified by the so-called Yoneda peak, which does not correspond to a specific orientation. This result suggests that PMMA-P*n*BA (as cast film) does not orient without thermal annealing. However, after thermal annealing for even 1 min, the scattering intensity around $q_y=0$, that is, the sides of the beam stop, became strong. In addition, two clear ring-shaped scattering patterns similar to the Debye–Scherrer rings were observed. Each scattering pattern can be assigned to scattering contributions arising from transmitted X-rays (denoted as T) or reflected X-rays (denoted as R). This phenomenon is typical of GISAXS measurements.[72,73] The scattering intensity around $q_y=0$ becomes stronger with increasing annealing time. This change in GISAXS patterns indicates the growth of the parallel orientation of the lamellar microphase-separated structure. To evaluate the degree of orientation quantitatively, the azimuthal angle dependence of the scattering intensity is normally analyzed in the case of normal-transmission SAXS. In the GISAXS geometry, it is quite difficult to analyze the degree of orientation in this way. It may be preferable to consider the scattering intensity ratio of $I_{parallel}$ (parallel lamellae) to $I_{in\text{-}plane}$ (perpendicular lamellae) to estimate the degree of orientation. The scattering intensity in-plane at $q_y=0.29$ is essentially produced by the overlapping scattering contributions of transmitted and reflected X-rays, and it also includes the Yoneda band. It is quite difficult to deconvolve the overlapping intensity into individual components. In addition, these scattering contributions to the in-plane intensity change as the incident angle α_i varies. Under the present experimental conditions, the GISAXS patterns of thin films with different annealing times were obtained

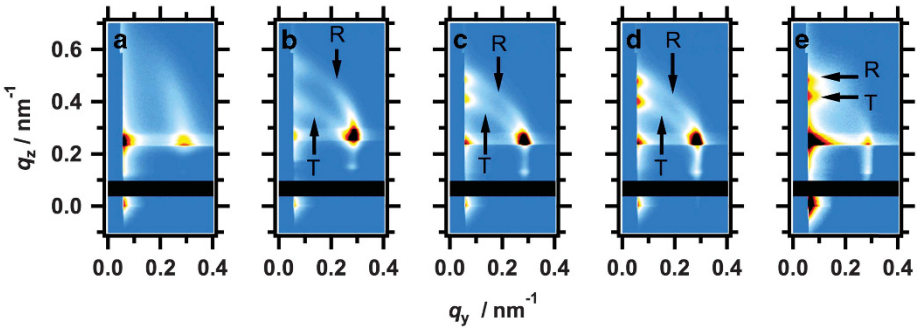

Figure 2 GISAXS patterns (hard X-ray, 1.488 Å) of PMMA-P*n*BA thin films as cast (**a**) and annealed at 160 °C for different annealing times, (**b**) 1, (**c**) 3, (**d**) 5 and (**e**) 10 min. R and T represent the scattering from the reflected and transmitted X-ray beam, respectively.

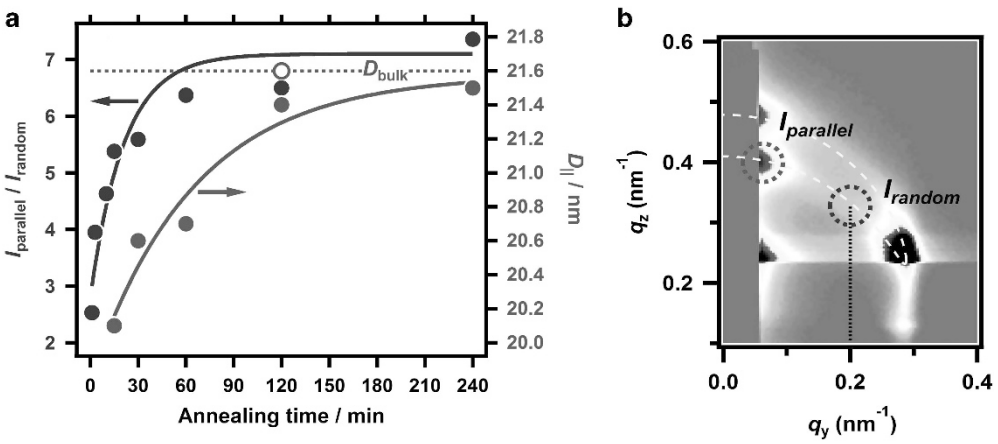

Figure 3 (**a**) Time evolution of the lamellar orientation (blue solid symbols) and the relaxation of the lamellar domain spacing (red filled symbols). The solid lines are drawn as a guide for the eyes. The dotted line indicates the $D_{\|}$ value of the bulk. The open circle shows the $D_{\|}$ value near the surface. The scattering intensity used for estimation of the apparent degree of orientation is shown in **b**. The intensity of the parallel and random components at fixed positions on the Debye–Scherrer-like ring arising from transmitted X-ray (bottom dashed curves, upper one is coming from reflected X-ray) was used. A full color version of this figure is available at *Polymer Journal* online.

independently, and each pattern was measured with different incident angles. In this situation, the change of the in-plane intensity depends not only on the orientation but also the degree of overlapping of the scatterings discussed above. Quantitative analysis of the degree of orientation still comes with difficulty because of these reasons. Thus, to discuss the orientation behavior qualitatively, the apparent scattering intensity of the parallel orientation ($I_{parallel} = I_{para}{}^{0} + I_{para,BG}$) was compared with the scattering intensity of a random orientation ($I_{random} = I_{ran}{}^{0} + I_{ran,BG}$), as shown in Figure 3b. The value of $I_{parallel}$ was read from nearest position to the beam stop (near a q_y value of 0). The value of I_{random} was obtained from the position where $q_y = 0.2\ nm^{-1}$ and a q_z position on the Debye–Scherrer-like ring (assuming a random orientation). Here, $I_{para}{}^{0}$ and $I_{ran}{}^{0}$ are true values of parallel and random components, respectively. Both experimentally obtained intensities ($I_{parallel}$ and I_{random}) include what are essentially background scatterings, $I_{para,BG}$ and $I_{ran,BG}$, respectively. The value of $I_{parallel}/I_{random}$ was used as a measure of the orientation behavior, although it is quite difficult to analyze the degree of the orientation from the value of $I_{parallel}/I_{random}$ in GISAXS quantitatively because of the different X-ray transmission and reflectivity values, which depend on the film thickness, surface roughness and incident angles (also background), and I_{random} is still somewhat variable under the present experimental condition. Figure 3a presents plots of the values of $I_{parallel}/I_{random}$ as a function of annealing time. Orientation is nearly complete after annealing at 160 °C for 60 min.

The GISAXS measurement provided structure information about the domain spacing of the lamellar morphology. The parallel lamellar structure preferentially forms as described above. The domain spacing ($D_{\|}$) of the lamellar structures with alignment parallel to the surface was estimated. To determine the accurate domain spacing, the distorted wave Born approximation (DWBA) was applied to the analysis of the GISAXS patterns. The scattering contributions from the transmitted X-rays (Transmission) and reflected X-rays (Reflection) are notable in the GISAXS measurement. The peak positions of each scattering component along the q_z direction can be estimated using DWBA as follows;[72–74]

$$q_z = \frac{2\pi}{\lambda}\left[\sin\alpha_i + \left\{\sin^2\alpha_c + \left[\frac{m\lambda}{D_{\|}} \mp \left(\sin^2\alpha_i - \sin^2\alpha_c\right)^{1/2}\right]^2\right\}^{1/2}\right] \quad (8)$$

where m represents the peak order, which is unity for this case. The upper (−) and lower (+) branches in the equation indicate the peak positions of the transmitted and reflected beams, respectively. Figure 4 shows the experimentally obtained Bragg spots as a function of the angle of incidence for PMMA-P*n*BA annealed for 240 min. When D was set to 21.5 nm, the calculation using Equation (8) gave the best fit for all Bragg spots, as shown by the dashed line in Figure 4. The values of $D_{\|}$ estimated in this way for all annealed samples were also plotted as a function of annealing time in Figure 3a. The value of $D_{\|}$

approached the domain spacing of the bulk sample (D_{bulk}, measured independently to be 21.6 nm, Supplementary Figure S3) with increasing annealing time. The domain spacing of the parallel-oriented structure was slightly smaller than that of the bulk, even after thermal annealing for 4 h. The polymer chains were fixed on the substrate, and the film thickness decreased during the rapid evaporation of the solvent. Consequently, the lamellar structure was deformed along the depth direction. However, thermal annealing induced the relaxation of the domain spacing. It seemed to take more than ~2 h to complete the relaxation of $D_{||}$ to the bulk value.

As is well known, the preferential wetting of surface and substrate interfaces has an important role in the orientation of thin films.[16,21] In this case, the surface energies of PMMA, P*n*BA and Si substrate are 41.1, 33.7 and 77.4 ± 0.5 mJ m^{-2}, respectively.[20] According to the surface free energies, it is predicted that PMMA segregates to the surface at the silicon substrate, while P*n*BA segregates to the air surface. As a result of preferential wetting, a parallel orientation of the lamellar morphology is induced at both the air and polymer/substrate interfaces and propagates through the entire film.[75] In fact, XPS measurements revealed that the molar fraction of P*n*BA at the surface was 80 mol% (repeat unit) in the cast film, and the P*n*BA component fully covered the surface even after annealing for only 60 s.

According to the results discussed here, the segregation of each component, orientation of the lamellae and relaxation of the domain spacing occurred on different time scales. It can be concluded that the P*n*BA first segregated at the air surface within 1 min of annealing (PMMA may have segregated at the interface). Second, the microphase-separated structure aligned parallel to the surface, followed by relaxation of the domain spacing. Because the estimation of the intensity ratio $I_{parallel}/I_{random}$ in a highly qualitative way includes a large uncertainty, we would like to provide as quantitative an interpretation of the observed behaviors as possible in the future.

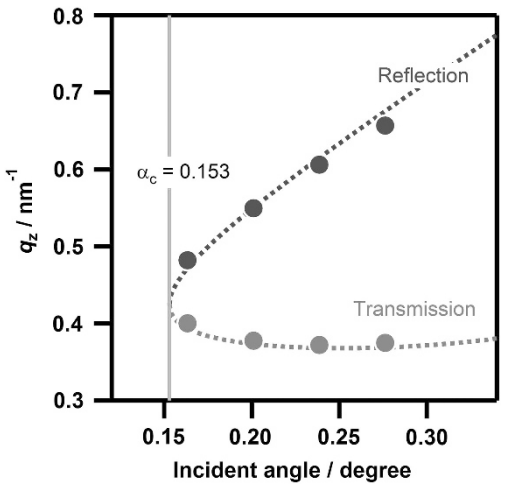

Figure 4 The incident angle dependence of the scattering positions along the q_z direction of PMMA-P*n*BA thin film annealed for 240 min with X-ray energy of 8.265 keV (corresponding to the wavelength of 1.5 Å). Red and blue symbols represent the spots arising from transmitted and reflected X-ray, respectively. Dashed lines are the simulated q_z using Equation (8) with a $D_{||}$ of 21.5 nm and an α_c of 0.153°. A full color version of this figure is available at *Polymer Journal* online.

Structure at near surface revealed by tender X-ray GISAXS measurement

It has been reported that polymer thin films have different mobilities that depend on the local region, that is, near the surface, in the interior, or near the polymer/substrate interface. It is quite intriguing to investigate whether depth dependence exists in the structure variation or, in other words, whether there is difference between the structure (orientation, morphology, *d* spacing and so on) in the vicinity of the surface and inside the film. Okuda *et al.*[63] and our group[64] have reported that tender X-ray GISAXS has the capability to perform depth-resolved analysis of the structure of thin films. In this study, tender X-ray GISAXS measurements of PMMA-P*n*BA thin films thermally annealed for 2 h were performed at various incident angles. As shown in Figures 5a and b, in the case where α_i was below α_c, the scattering (marked arrows) of the lamellar structure oriented parallel to the substrate was considerably diffused and broadened, while in the case where α_i was greater than α_c, the scattering became clear and sharp. The one-dimensional scattering profiles vertically cut at q_y as close to the beam stop as possible are summarized in Figure 5c. As discussed above, the scattering peaks are assigned to transmission (denoted as T) and reflection (denoted as R). The peak position shifts and full width at half maximum (FWHM) magnitudes varied with the change of the incident angle. The shifts of the peak position can be explained using the DWBA (Equation (8)), as shown previously in Figure 4, while the change of the FWHM can be discussed in terms of the change of penetration depth of X-rays.[63,64]

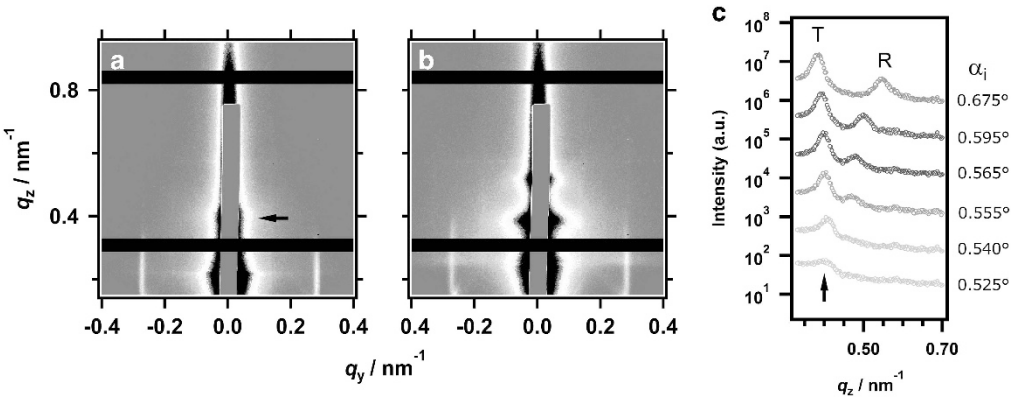

Figure 5 Tender X-ray (2.40 keV) GISAXS patterns of PMMA-P*n*BA thin film annealed at 160 °C for 2 h measured at angles of incidence (**a**) 0.525° and (**b**) 0.625°. (**c**) One-dimensional profiles vertically cut at q_y in the vicinity of the beam stop obtained at various incident angles α_i. Each profile is shifted vertically to avoid overlapping. A full color version of this figure is available at *Polymer Journal* online.

The FWHM depends on the grain size of a crystal as expressed with the Laue function, $L(q)$

$$L(q_z) = \sum_N \exp\left(iNq_Z \cdot D_\parallel\right) = \frac{\sin\left[(N+1)q_z \cdot D_\parallel/2\right]}{\sin\left[q_z \cdot D_\parallel/2\right]}, \quad (9)$$

where N is the number of the reflection plane. Here, the attenuation decay of the X-rays must be considered, that is, the X-ray wave decays exponentially. The Laue function can be re-expressed as

$$L(q_z) = \sum_N \frac{\sin\left[(N+1)q_z D_\parallel/2\right]}{\sin\left[q_z D_\parallel/2\right]} \exp\left[-\frac{ND_\parallel}{2\Lambda}\right] \quad (10)$$

Because the scattering intensity is proportional to the square of the Laue function, the FWHM can be calculated simply.

The FWHMs along the q_z direction obtained from the scattering peak of $D_\parallel$ (Transmission) are plotted as a function of the incident X-ray in Figure 6. As shown in Figure 6, the FWHM decreased remarkably in the vicinity of the critical angle of total reflection. Furthermore, the FWHM calculated using Equation (10) is also plotted in Figure 6. The calculated value also decreases drastically near the critical angle, indicating an identical trend to that observed in the experimental values. The experimental values are in accord with the calculated values for increasing penetration depth Λ given by Equation (4), indicating that the penetration depth can be controlled in agreement with the theory. Therefore, we conclude that the depth-resolved analysis was performed completely for the various incident angles considered in this measurement.

In the case of GISAXS measurements utilizing soft X-rays, the effect of large Ewald sphere curvature on the GISAXS pattern cannot be neglected. Hence the curvature may affect the peak position and scattering intensity (distorted scattering pattern).[76] If the curvature strongly affects the scattering peak positions, Equation (8) must be modified. Structure analysis of the same specimen (thermally annealed for 2 h) using Equation (8) was performed to confirm whether Equation (8) works out without any modification. Analysis of the incidence dependence of the scattering positions observed in Figure 5c using Equation (8) gave the same structural parameter, $D_\parallel = 21.4$ (inside the film), that was obtained in the case of an X-ray energy of 2.40 keV (Supplementary Figure S5). Thus, it was concluded that Equation (8) worked well even in the tender X-ray regime within the observed q-range in this article.

Near the critical angle, surface-sensitive measurements are possible, as calculated by Equation (4) (Figure 1). When α_i is below α_c, X-ray waves reach the film surface but cannot propagate into the film. Only the evanescent wave can penetrate from the surface into the film. In this situation, the experimentally observed scattering spot α_z along the q_z direction is given by the sum of the incident angle α_i and the scattering angle α_s derived from the period of the observed structure. Thus, α_s can be expressed as

$$\alpha_s = \alpha_z - \alpha_i \quad (11)$$

Using Equation (11), the true q_z value of the lamellar structure oriented parallel to the surface can be estimated using the experimentally observed peaks, that is, $D_\parallel$ can be estimated. In the case where α_i was 0.525° (corresponding to a Λ of 32.4 nm), $D_\parallel$ was estimated to be 21.6 nm, which is equal to the 21.6 nm value of the bulk sample. The value of $D_\parallel$ near the surface is larger than the 21.4 nm value obtained from the DWBA simulation (inside the film). This result indicates that the domain spacing in the vicinity of the film surface preceded was relaxed to that of the interior. As reported previously, polymer chains near the surface possess higher mobility (lower glass transition temperature or viscosity).[77–79] Moreover, the lamellar structure begins to orient from both the air/polymer and polymer/substrate interfaces, induced by segregation of one component of the BCP. Therefore, it can be concluded that the faster relaxation of the d spacing ($D_\parallel$) of the lamellar structure near the surface, causing the D value of the bulk to be reached, was caused by the faster segregation of the P*n*BA component at the surface and the higher mobility of the polymer chains in the vicinity of the surface.

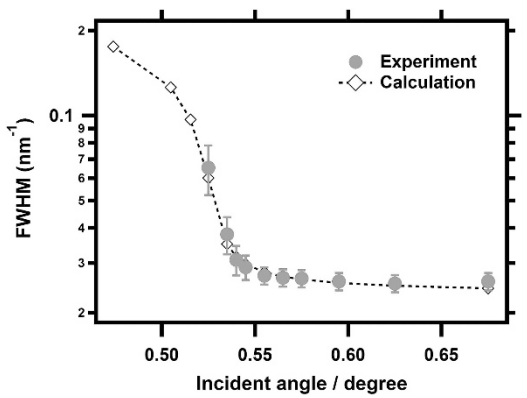

Figure 6 FWHM values of Bragg peak of $D_\parallel$ obtained experimentally (filled circles) and calculated (diamond and dashed line) using Equation (10). A full color version of this figure is available at *Polymer Journal* online.

CONCLUSION

We investigated the orientation behavior and the domain spacing relaxation of the phase-separated structure of PMMA-P*n*BA thin films using GISAXS. The PMMA-P*n*BA formed a lamellar structure, and the lamellar structure was aligned parallel to the substrate after thermal annealing. XPS measurements indicated that the segregation of the P*n*BA (PMMA) component occurred rapidly, within 1 min after annealing at 160 °C. The parallel orientation of the lamellar structure was observed successfully, and the domain spacing $D_\parallel$ was analyzed by the DWBA calculation. GISAXS measurements revealed that the apparent degree of orientation and the value of $D_\parallel$ increased with annealing time, while the domain spacing relaxation took a longer time than the orientation of the lamellae of the BCP. Moreover, we conducted low-energy GISAXS (tender X-ray) to enable the in-depth profiling of the microphase-separated structure. It was found that $D_\parallel$ in the vicinity of the surface was larger than inside the film, which indicates that the domain spacing near the surface relaxed faster than the inside, a phenomenon that arises from the higher mobility of the polymer chains. If the orientation behavior and precise time-dependent d spacing are analyzed more quantitatively, the local time scale of those attributes, which are dependent on the region, for example, near the surface or near the substrate (exhibiting spatial inhomogeneity) in the film will be discussed more precisely in future works.

CONFLICT OF INTEREST

The authors declare no conflict of interest.

ACKNOWLEDGEMENTS

This research was supported by the Ministry of Education, Culture, Sports, Science and Technology (MEXT) in Japan, Grant-in-Aid for Scientific Research (C) (26410132, 2014). GISAXS measurements were performed at the Photon Factory of the High Energy Accelerator Research Organization (approval 2014G169) and at the SPring-8 facility (approval 2014A7214, 2014B7264,

2015A7214). Furthermore, we thank Professor Noriyuki Igarashi and Professor Nobutaka Shimizu for their kind and dedicated support of low energy GISAXS at the PF.

1 Singh, G., Yager, K., Berry, B., Kim, H.-C. & Karim, A. Dynamic thermal field-induced gradient soft-shear for highly oriented block copolymer thin films. *ACS Nano* **6**, 10335–10342 (2012).
2 Luo, Y., Montarnal, D., Kim, S., Shi, W., Barteau, K. P., Pester, C. W., Hustad, P. D., Christianson, M. D., Fredrickson, G. H., Kramer, E. J. & Hawker, C. J. Poly (dimethylsiloxane-*b*-methyl methacrylate): a promising candidate for Sub-10 nm patterning. *Macromolecules* **48**, 3422–3430 (2015).
3 Gu, W., Zhao, H., Wei, Q., Coughlin, E. B., Theato, P. & Russell, T. P. Line patterns from cylinder-forming photocleavable block copolymers. *Adv. Mater.* **25**, 4690–4695 (2013).
4 Zhang, Q., Cirpan, A., Russell, T. P. & Emrick, T. Donor-acceptor poly (thiophene-block-perylene diimide) copolymers: synthesis and solar cell fabrication. *Macromolecules* **42**, 1079–1082 (2009).
5 Sun, S. S., Zhang, C., Ledbetter, A., Choi, S., Seo, K., Bonner, C. E. Jr, Dress, M. & Sariciftchi, N. S. Photovoltaic enhancement of organic solar cells by a bridged donor-acceptor block copolymer approach. *Appl. Phys. Lett.* **90**, 043117 (2007).
6 Crossland, E. J. W., Kamperman, M., Nedelcu, M., Ducati, C., Wiesner, U., Smilges, D.-M., Toombes, G. E. S., Hilmyer, M. A., Ludwigs, S., Steiner, U. & Snaith, H. J. A bicontinuous double gyroid hybrid solar cell. *Nano Lett.* **9**, 2807–2812 (2008).
7 Wan, L.-S., Li, J.-W., Ke, B.-B. & Xu, Z.-K. Ordered microporous membranes template by breath figures for size-selective separation. *J. Am. Chem. Soc.* **134**, 95–98 (2012).
8 Jeong, U, Ryu, D. Y., Kim, J. K., Kim, D. H., Wu, X. & Russell, T. P. Precise control of nanopore size in thin film using mixtures of asymmetric block copolymer and homopolymer. *Macromolecules* **36**, 10126–10129 (2003).
9 Brown, H. R. Effect of a diblock copolymer on the adhesion between incompatible polymers. *Macromolecules* **22**, 2859–2860 (1989).
10 Coumans, W. J., Heikens, D. & Sjoerdsmas, D. Dilatometric investigation of deformation mechanisms in polystyrene-polyethylene block copolymer blends: correlation between Poisson ratio and adhesion. *Polymer* **21**, 103–108 (1980).
11 Matsen, M. W. & Bates, F. S. Unifying weak- and strong-segregation block copolymer theories. *Macromolecules* **29**, 1091–1098 (1996).
12 Matsen, M. W. & Schick, M. Stable and unstable phases of a diblock copolymer melt. *Phys. Rev. Lett.* **72**, 2660–2663 (1994).
13 Bates, F. S. & Fredrickson, G. H. Block copolymer thermodynamics: theory and experiment. *Annu. Rev. Phys. Chem.* **41**, 525–557 (1990).
14 Stein, G. E., Kramer, E. J., Li, X. & Wang, J. Layering transitions in thin films of spherical-domain block copolymers. *Macromolecules* **40**, 2453–2460 (2007).
15 Suh, H. S., Kang, H., Nealey, P. F. & Char, K. Thickness dependence of neutral parameter windows for perpendicularly oriented block copolymer thin films. *Macromolecules* **43**, 4744–4751 (2010).
16 Albert, J. & Epps, T. H. Self-assembly of block copolymer thin films. *Mater. Today* **13**, 24–44 (2010).
17 Jung, J., Park, H. W., Lee, S., Lee, H., Chang, T., Matsunaga, T. & Jinnai, H. Effect of film thickness on the phase behaviors of diblock copolymer thin film. *ACS Nano* **4**, 3109–3116 (2010).
18 Luo, M., Seppala, J. E., Albert, J. N. L., Lewis, R., Mahadevapuram, N., Stein, G. E. & Epps, T. H. Manipulating nanoscale morphologies in cylinder-forming poly (styrene-*b*-isoprene-*b*-styrene) thin films using film thickness and substrate surface chemistry gradient. *Macromolecules* **46**, 1803–1811 (2013).
19 Kim, S. O., Solak, H. H., Stoykovich, M. P., Ferrier, N. J., Pablo, J. J. & Nealey, P. F. Epitaxial self-assembly of block copolymers on lithographically defined nanopatterned substrates. *Nature* **424**, 411–414 (2003).
20 Shelton, C. K. & Epps, T. H. Decoupling substrate surface interactions in block polymer thin film self-assembly. *Macromolecules* **48**, 4572–4580 (2015).
21 Mansky, P., Liu, Y., Huang, E., Russell, T. P. & Hawker, C. Controlling polymer-surface interactions with random copolymer brushes. *Science* **275**, 1458–1460 (1997).
22 Han, E, Stuen, K. O., Leolukman, M., Liu, C.-C., Nealy, P. F. & Gopalan, P. Perpendicular orientation of domains in cylinder-forming block copolymer thick films by controlled interfacial interactions. *Macromolecules* **42**, 4896–4901 (2009).
23 Khanna, V., Cochran, E. W., Hexemer, A., Stein, G. E., Fredrickson, G. H., Kramer, E. J., Li, X., Wang, J. & Hahn, S. F. Effect of chain architecture and surface energies on the ordering behavior of lamellar and cylinder forming block copolymers. *Macromolecules* **39**, 9346–9356 (2006).
24 Sohn, B. H. & Yun, S. H. Perpendicular lamellae induced at the interface of neutral self-assembled monolayers in thin diblock copolymer films. *Polymer* **43**, 2507–2512 (2002).
25 Park, S., Lee, D. H., Xu, J., Kim, B., Hong, S. W., Jeong, U., Xu, T. & Russell, T. P. Macroscopic 10-terabit–per–square-inch arrays from block copolymers with lateral order. *Science* **323**, 1030–1033 (2009).
26 Sivaniah, E., Hayashi, Y., Iino, M., Hashimoto, T. & Fukunaga, K. Observation of perpendicular orientation in symmetric diblock copolymer thin films on rough substrates. *Macromolecules* **36**, 5894–5896 (2003).
27 Sivaniah, E., Hayashi, Y., Matsubara, S., Kiyono, S., Hashimoto, T., Fukunaga, K., Kramer, E. J. & Mates, T. Symmetric Diblock copolymer thin films on rough substrates. Kinetics and structure formation in pure block copolymer thin films. *Macromolecules* **38**, 1837–1849 (2005).
28 Singh, G., Yager, K. G., Berry, B., Kim, H.-C. & Karim, A. Dynamic thermal field-induced gradient soft-shear for highly oriented block copolymer thin films. *ACS Nano* **6**, 10335–10342 (2012).
29 Chremos, A., Chaikin, P. M., Register, R. A. & Panagiotopoulos, A. Sphere-to-cylinder transitions in thin films of diblock copolymers under shear: the role of wetting layers. *Macromolecules* **45**, 4406–4415 (2012).
30 Angelescu, D. E., Waller, J. H., Adamson, D. H., Deshpande, P., Chou, S. Y., Register, R. A. & Chaikin, P. M. Macroscopic orientation of block cylinders in single-layer films by Shearing. *Adv. Mater.* **16**, 1736–1740 (2004).
31 Hong, Y.-R., Adamson, D. H., Chaikin, P. M. & Register, R. A. Shear-induced sphere-to-cylinder transition in diblock copolymer thin films. *Soft Matter* **5**, 1687–1691 (2009).
32 Fukuhara, K., Nagano, S., Hara, M. & Seki, T. Free-surface molecular command systems for photoalignment of liquid crystalline materials. *Nat. Commun.* **5**, 3320 (2014).
33 Sano, M., Nakamura, S., Hara, M., Nagano, S., Shinohara, Y., Amemiya, Y. & Seki, T. Pathways toward photoinduced alignment switching in liquid crystalline block copolymer films. *Macromolecules* **47**, 7178–7186 (2014).
34 Xu, T., Zvelindovsky, A. V., Sevink, G. J. A., Lyakhova, K. S., Jinnai, H. & Russell, T. P. Electric field alignment of asymmetric diblock copolymer thin films. *Macromolecules* **38**, 10788–10798 (2005).
35 Cui, G., Ohya, S., Matsutani, T., Nagano, S., Dohi, T., Nakamura, S., Sakurai, S., Miyazaki, T. & Yamamoto, K. Perpendicular orientation of sub-10 nm channels in polystyrene-b-poly(4-hydroxyl styrene)/PEG oligomer blend thin films. *Nanoscale* **5**, 6713–6719 (2013).
36 Cui, G., Fujikawa, M., Nagano, S., Sano, M., Takase, H., Miyazaki, T., Sakurai, S. & Yamamoto, K. Perpendicular oriented cylinders via directional coalescence of spheres embedded in block copolymer films induced by solvent annealing. *Polymer* **55**, 1601–1608 (2014).
37 Gu, W., Xu, J., Kim, J.-K., Hong, S. W., Wei, X., Yang, X., Lee, K. Y., Kuo, D. S., Xiao, S. & Russell, T. P. Solvent-assisted directed self-assembly of spherical microdomain block copolymers to high areal density arrays. *Adv. Mater.* **25**, 3677–3682 (2013).
38 Kim, S. H., Misner, M. J., Yang, L., Gang, O., Ocko, B. M. & Russell, T. P. Salt complexation in block copolymer thin films. *Macromolecules* **39**, 8473–8479 (2006).
39 Jeong, J. W., Park, W. I., Kim, M.-J., Ross, C. A. & Jung, Y. S. Highly tunable self-assembled nanostructures from a poly(2-vinylpyridine-*b*-dimethylsiloxane) block copolymer. *Nano Lett.* **11**, 4095–4101 (2011).
40 Park, S., Wang, J.-Y., Kim, B., Xu, J. & Russell, T. P. A simple route to highly oriented and ordered nanoporous block copolymer templates. *ACS Nano* **2**, 766–772 (2008).
41 She, M.-S., Lo, T.-Y. & Ho, R.-M. Long-range ordering of block copolymer cylinders driven by combining thermal annealing and substrate functionalization. *ACS Nano* **7**, 2000–2011 (2013).
42 Edwards, E., Stoykovich, M. P., Müller, M., Solak, H. H., Pablo, J. J. & Nealey, P. F. Mechanism and kinetics of ordering in diblock copolymer thin films on chemically nanopatterned substrates. *J. Polym. Sci. B* **43**, 3444–3459 (2005).
43 van Dijk, M. A. & van den Berg, R. Ordering phenomena in thin block copolymer films studied using atomic force microscopy. *Macromolecules* **28**, 6773–6778 (1995).
44 Collin, B., Chatenay, D., Coulon, G., Ausserre, D. & Gallot, Y. Ordering of copolymer thin films as revealed by atomic force microscopy. *Macromolecules* **25**, 1621–1622 (1992).
45 Yokoyama, H., Kramer, E. J., Rafailovich, M. H., Sokolov, J. & Schwarz, S. A. Structure and diffusion of asymmetric diblock copolymers in thin films: a dynamic secondary ion mass spectrometry study. *Macromolecules* **31**, 8826–8830 (1998).
46 Coulon, G., Russell, T. P., Deline, V. R. & Green, P. F. Surface-induced orientation of symmetric, diblock copolymers: a secondary ion mass-spectrometry study. *Macromolecules* **22**, 2581–2589 (1989).
47 Zhang, J., Posselt, D., Smilgies, D.-M., Perlich, J., Kyriakos, K., Jaksch, S. & Papadakis, C. M. Lamellar diblock copolymer thin films during solvent vapor annealing studied by GISAXS: different behavior of parallel and perpendicular lamellae. *Macromolecules* **47**, 5711–5718 (2014).
48 Müller-Buschbaum, P. Grazing incidence small-angle X-ray scattering: an advanced scattering technique for the investigation of nanostructured polymer films. *Anal. Bioanal. Chem.* **376**, 3–10 (2003).
49 Choi, S., Kim, E., Ahn, H., Naidu, S., Lee, Y., Ryu, D. Y., Hawker, C. J. & Russell, T. P. Lamellar microdomain orientation and phase transition of polystyrene-*b*-poly(methyl methacrylate) films by controlled interfacial interactions. *Soft Matter* **8**, 3463–3469 (2012).
50 Müller-Buschbaum, P., Maurer, E., Bauer, E. & Cubitt, R. Surface versus confinement induced morphology transition in triblock copolymer films: a grazing incidence small angle neutron scattering investigation. *Langmuir* **22**, 9295–9303 (2006).
51 Busch, P., Posselt, D., Smilgies, D., Rauscher, M. & Papadakis, C. Inner structure of thin films of lamellar poly(styrene-*b*-butadiene) diblock copolymers as revealed by grazing-incidence small-angle scattering. *Macromolecules* **40**, 630–640 (2007).
52 Müller-Buschbaum, P., Schulz, L., Metwalli, E., Moulin, J.-F. & Cubitt, R. Lateral structures of buried interfaces in ABA-type triblock copolymer films. *Langmuir* **24**, 7639–7644 (2008).
53 Niihara, K., Matsuwaki, U., Torikai, N., Atarashi, H., Tanaka, K. & Jinnai, H. A novel structural analysis for a cylinder-forming block copolymer thin film using neutron reflectivity aided by transmission electron microtomography. *Macromolecules* **40**, 6940–6946 (2007).
54 Noro, A., Okuda, M., Odamaki, F., Kawaguchi, D., Torikai, N., Takano, A. & Matsushita, Y. Chain localization and interfacial thickness in microphase-separated

structures of block copolymers with variable composition distributions. *Macromolecules* **39**, 7654–7661 (2006).
55 Tokarev, I., Krenek, R., Burkov, Y., Schmeisser, D., Sidorenko, A., Minko, S. & Stamm, M. Microphase separation in thin films of poly (styrene-block-4-vinylpyridine) copolymer-2-(4'-hydroxybenzeneazo) benzoic acid assembly. *Macromolecules* **38**, 507–516 (2005).
56 Thomas, H. R. & O'Malley, J. J. Surface studies on multicomponent polymer systems by X-ray photoelectron spectroscopy. Polystyrene/poly (ethylene oxide) diblock copolymers. *Macromolecules* **12**, 323–329 (1979).
57 Gu, X., Gunkel, I., Hexemer, A., Gu, W. & Russell, T. P. An in situ grazing incidence X-ray scattering study of block copolymer thin films during solvent vapor annealing. *Adv. Mater.* **26**, 273–281 (2014).
58 Albert, J. N., Baney, M. J., Stafford, C. M., Kelly, J. Y. & Epps, T. H. Generation of monolayer gradients in surface energy and surface chemistry for block copolymer thin film studies. *ACS Nano* **3**, 3977–3986 (2009).
59 Kipnusu, W. K., Elmahdy, M. M., Tress, M., Fuchs, M., Mapesa, E. U., Smilgies, D.-M., Zhang, J., Papadakis, C. M. & Kremer, F. Molecular order and dynamics of nanometric thin layers of poly (styrene-b-1, 4-isoprene) diblock copolymers. *Macromolecules* **46**, 9729–9737 (2013).
60 Xu, T., Hawker, C. & Russell, T. P. Interfacial interaction dependence of microdomain orientation in diblock copolymer thin films. *Macromolecules* **38**, 2802–2805 (2005)
61 Terlier, T., Tiron, R., Gharbi, A., Chevalier, X., Veillerot, M., Martinez, E. & Barnes, J.-P. Investigation of block depth distribution in PS-b-PMMA block copolymer using ultra-low-energy cesium sputtering in TOF-SIMA. *Surf. Interface Anal.* **46**, 83–91 (2014).
62 Busch, P., Rauscher, M., Moulin, J.-F. & Müller-Buschbaum, P. Debye–Scherrer rings from block copolymer films with powder-like order. *J. Appl. Cryst.* **44**, 370–379 (2011).
63 Okuda, H., Takeshita, K., Ochiai, S., Sakurai, S. & Kitajima, Y. Near-surface relaxation structure of annealed block copolymer film on Si substrates examined by grazing-incidence small-angle scattering utilizing soft X-rays. *J. Appl. Cryst.* **44**, 380–384 (2011).
64 Saito, I., Miyazaki, T. & Yamamoto, K. Depth-resolved structure analysis of cylindrical microdomain in block copolymer thin film by grazing-incidence small angle X-ray scattering utilizing low energy X-ray. *Macromolecules* **48**, 8190–8196 (2015).
65 Matyjaszewski, K. Atom transfer radical polymerization (ATRP): current status and future perspectives. *Macromolecules* **45**, 4015–4039 (2012).
66 Cui, G., Fujikawa, M., Nagano, S., Shimokita, K., Miyazaki, T., Sakurai, S. & Yamamoto, K. Macroscopic alignment of cylinders via directional coalescence of spheres along annealing solvent permeation directions in block copolymer thick films. *Macromolecules* **47**, 5989–5999 (2014).
67 Ogawa, H., Masunaga, H., Sasaki, S., Goto, S., Tanaka, T., Seike, T., Takahashi, S., Takeshita, K., Nariyama, N., Ohashi, H., Ohata, T., Furukawa, Y., Matsushita, T., Ishizawa, Y., Yagi, N., Takata, M., Kitamura, H., Takahara, A., Sakurai, K., Tashiro, K., Kanaya, T., Amemiya, Y., Horie, K., Takenaka, M., Jinnai, H., Okuda, H., Akiba, I., Takahashi, I., Yamamoto, K., Hikosaka, M., Sakurai, S., Shinohara, Y., Sugihara, Y. & Okada, A. Experimental station for multiscale surface structural analyses of soft-material films at SPring-8 via a GISWAX/GIXD/XR-integrated system. *Polym. J.* **45**, 109–116 (2012).
68 Masunaga, H., Ogawa, H., Takano, T., Sasaki, S., Goto, S., Tanaka, T., Seike, T., Takahashi, S., Takeshita, K., Nariyama, N., Ohashi, H., Ohata, T., Furukawa, Y., Matsushita, T., Ishizawa, Y., Yagi, N., Takata, M., Kitamura, H., Sakurai, K., Tashiro, K., Takahara, A., Amamiya, Y., Horie, K., Takenaka, M., Kanaya, T., Jinnai, H., Okuda, H., Akiba, I., Takahashi, I., Yamamoto, K., Hikosaka, M., Sakurai, S., Shinohara, Y., Okada, A. & Sugihara, Y. Multipurpose soft-material SAXS/WAXS/GISAXS beamline at SPring-8. *Polym. J.* **43**, 471–477 (2011).
69 Ruderer, M. A., Wang, C., Schaible, E., Hexemer, A., Xu, T. & Müller-Buschbaum, P. Morphology and optical properties of P3HT:MEH-CN-PPV blend films. *Macromolecules* **46**, 4491–4501 (2013).
70 Virgili, J. M., Tao, Y., Kortright, J. B., Balsara, N. P. & Segalman, R. A. Analysis of order formation in block copolymer thin films using resonant soft X-ray scattering. *Macromolecules* **40**, 2092–2099 (2007).
71 Beiglböck, W., Ehlers, J., Hepp, K., Weidenmüller, H., Beig, R., Domcke, W., Englert, B.-G., Frisch, U., Hänggi, P., Hasinger, G., Hillebrandt, W., Jaffe, R., Janke, W., von Löhneysen, Mangano, M., Raimond, J.-M., Sornette, D., Theisen, S., Weise, W., Zittartz, J., Guinea, F., Vollhardt, D., Daillant, J. & Gibaud, A. in *X-ray and Neutron Reflectivity: Principles and Applications*, Lecture Notes in Physics 770 (eds Daillant, J. & Gibaud, A.) (Springer, Berlin, Heidelberg, Germany, 2009)
72 Yoon, J., Yang, S. Y., Lee, B., Joo, W., Heo, K., Kim, J. K. & Ree, M. Nondestructive quantitative synchrotron grazing incidence X-ray scattering analysis of cylindrical nanostructures in supported thin films. *J. Appl. Cryst.* **40**, 305–312 (2007).
73 Busch, P., Rauscher, M., Smilgies, D.-M., Posselt, D. & Papadakis, C. M. Grazing-incidence small-angle X-ray scattering from thin polymer films with lamellar structures – the scattering cross section in the distorted-wave Born approximation. *J Appl. Cryst.* **39**, 433–442 (2006).
74 Lee, B., Park, I., Yoon, J., Park, S., Kim, J., Kim, K.-W., Chang, T. & Ree, M. Structural analysis of block copolymer thin films with grazing incidence small-angle X-ray scattering. *Macromolecules* **38**, 4311–4323 (2005).
75 Russell, T. P., Coulon, G., Deline, V. R. & Miller, D. C. Characteristics of the surface-induced orientation for symmetric diblock PS/PMMA copolymers. *Macromolecules* **22**, 4600–4604 (1989).
76 Yamamoto, T., Okuda, H., Takeshita, K., Usami, N., Kitajima, Y. & Ogawa, H. Grazing-incidence small-angle X-ray scattering from Ge nanodots self-organized on Si (001) examined with soft X-rays. *J. Synchrotron Rad.* **21**, 161–164 (2014).
77 Kawaguchi, D., Tanaka, K., Kajiyama, T., Takahara, A. & Tasaki, S. Mobility gradient in surface region of monodisperse polystyrene films. *Macromolecules* **36**, 1235–1240 (2003).
78 Kajiyama, T., Tanaka, K. & Takahara, A. Depth dependence of the surface glass transition temperature of a poly (styrene-block-methyl methacrylate) diblock copolymer film on the basis of temperature-dependent X-ray photoelectron spectroscopy. *Macromolecules* **28**, 3482–3484 (1995)
79 Inoue, R., Kawashima, K., Matsui, K. & Nakamura, M. Interfacial properties of polystyrene thin films as revealed by neutron reflectivity. *Phys. Rev. E* **84**, 031802 (2011).

Supplementary Information accompanies the paper on Polymer Journal website (http://www.nature.com/pj)